JOURNAL OF SOLID STATE CHEMISTRY 115, 427–434 (1995)

Structure and Physical Properties of the Barium Niobium Sulfides $BaNbS_3$ and $BaNb_{0.8}S_{3-\delta}$

Sung-Jin Kim,[1] Hyun-Sook Bae, and Kyeong-Ae Yee

Department of Chemistry, Ewha Womans University, Seoul, Korea

Jin-Ho Choy and Dong-Kuk Kim

Department of Chemistry, Seoul National University, Seoul, Korea

and

Nam-Hwi Hur

Korea Research Institute of Standards and Science

Received March 28, 1994; in revised form June 28, 1994; accepted June 30, 1994

$BaNb_{0.8}S_{3-\delta}$ and $BaNbS_3$ were prepared by heating desired amounts of $BaCO_3$ and Nb_2O_5 under CS_2/N_2 flow. We found that nominal composition of $BaNb_{0.8}S$ has sulfur defect, and therefore should be written as $BaNb_{0.8}S_{3-\delta}$. XANES experiments of Nb *K*-edges and XPS experiments proved that the oxidation state of Nb is the same in $BaNb_{0.8}S_{3-\delta}$ and $BaNbS_3$. To understand their structures, the electronic and physical properties of the $BaMX_3$ (M = V, Nb, X = S; M = Ta, X = S, Se) phases are compared. In spite of their structural similarity, they exhibit rather different physical properties. It has been known that $BaVS_3$ is a metal and undergoes a metal to semiconductor transition at 130 K, and this phase shows the ferro antiferromagnetic transition at a lower temperature. However, $BaNbS_3$ and $BaTaS_3$ are diamagnetic semiconductors at room temperature. The major factor stabilizing the semiconducting state for $BaTaX_3$ and $BaNbS_3$ may be a large spin–orbit coupling rather than a structural distortion.

INTRODUCTION

Ternary sulfides and selenides of the stoichiometry $BaMX_3$(M = Ti, Nb, X = S; M = V, Ta, X = S, Se) (1–11) are isostructual with $AMCl_3$ system (M = V, Cr, Mn, Fe, Co, Ni, Cu; A = Cs, Rb, $N(CH_3)_4$) (12–29), and have been known for more than 20 years. All of these chalcogenides consist of face-sharing octahedra along the chain axis and each metal is located at the center of a face-sharing chalcogen octahedron. The crystal structure of $BaMX_3$ at room temperature is hexagonal with space group of $P6_3/mmc$, and the chains are separated by large barium ions. The intrachain metal–metal distances are 2.81–2.87 Å, which are short enough to form metal–metal bonds (2, 30), but the interchain metal–metal distances are long, with the range of 6.7–7.0 Å.

In spite of the structural similarity, the face-sharing octahedral chains of the chalcogenides $BaMX_3$ and the chlorides $AMCl_3$ exhibit different physical properties. While the chlorides are magnetic insulators, the sulfides are either metals or semiconductors. Whangbo *et al.* studied how the chlorides and sulfides have different properties (31) in great detail. However, it has not been fully understood why $BaVX_3$ (X = S, Se) systems behave differently from their congeners $BaNbS_3$ and $BaTaX_3$.

$BaVS_3$ shows a metallic behavior and a paramagnetism at room temperature. It can be said that one d electron (V^{4+}) per each metal makes this system behave paramagnetic. As the temperature decreases, its resistivity increases mildly in the temperature range between 130 and 70 K, and sharply between 70 and 4.2 K (32). The sharp rise in the resistivity at 70 K coincides with the paramagnetic to antiferromagnetic transition and is not caused by a structural phase transition such as a Peierls distortion (33, 34). However, $BaVS_3$ undergoes a structural distortion from hexagonal to orthorhombic near 250 K (8, 10, 11), which makes the V^{4+} ions slightly zigzagging but causes no drastic change in the conductivity.

$BaTaX_3$ and $BaNbX_3$ systems are diamagnetic semiconductors (2, 35). It is speculated by Geertsma *et al.* (36) that the observed semiconductivity of $BaTaS_3$ results from the large spin–orbit coupling constant of Ta^{4+}, which stabilizes the semiconducting state. In that case, the ground state is fourfold degenerate with zero magnetic moment. Therefore, $BaTaS_3$ is a diamagnetic semiconductor at room temperature. However, the observed

[1] To whom correspondence should be addressed.

0022-4596/95 $6.00

diamagnetism of this quasi-one-dimensional system with one d-electron per MX_3^{2-} unit prompted us to reinvestigate if Peierls distortion favors over spin–orbit coupling, especially in $BaNbS_3$.

In the present work, the structures, the oxidation states of Nb and the electronic properties of $BaNbS_3$ and $BaNb_{0.8}S_3$ are investigated on the basis of X-ray diffraction, magnetic susceptibility, and electrical resistivity measurements. We also carried out X-ray photoelectron spectroscopy (XPS) and X-ray absorption near-edge structure (XANES) studies.

Previously, it was reported that $BaMS_3$ (M = Nb, Ta) phases are always nonstoichiometric (i.e., $BaM_{0.8}S_3$), with unidentified MS_2 phase (35). Further, it was suggested that $BaM_{0.8}S_3$ (M = Nb, Ta) contains M^{5+} ions thereby rationalizing the observed diamagnetic semiconduting behavior. However, the present work reports different conclusion.

EXPERIMENTAL

$BaM_{1-x}S_3$ (M = Nb, Ta, x = 0.0, 0.2) samples were prepared by heating desired amounts of $BaCO_3$ and Nb_2O_5 (or Ta_2O_5) at 800°C for 24 hr under CS_2/N_2 flow. Products were ground and reheated under the same condition from 24 to 48 hr to ensure complete reactions.

Powder X-ray diffraction measurements were carried out at room temperature using a Siemens X-ray diffractometer and Co$K\alpha$ radiation. X-ray diffraction data were analyzed using a Rietveld-type full-profile refinement technique with a measuring step of 0.02° (in 2θ) and a counting time of 6 sec. For a low-temperature X-ray study, powder samples were mixed with nitrocellulose and spread on sample holder with thermocouple attached. A temperature of 210 K was reached by blowing liquid nitrogen directly onto the sample.

Electrical resistivities were measured using the standard four-probe method, in which four wires were connected to sintered pellets. Sintered samples were prepared by heating pressed pellets in an evacuated quartz tube at 500°C for 5 hr. For the low temperature (liquid helium range) experiments, four wires were connected to the sample by indium contacts. For higher temperature (from room temperature to 750 K) experiments, tungsten wires were pressed to the sample directly and measurements were carried out under an argon atmosphere. DC magnetic susceptibilities were measured at temperatures ranging from 5 to 300 K using a Quantum Design SQUID magnetometer.

XPS experiments were carried out with a Surface Science Instrument. Samples were mounted on an aluminium plate. Nonmonochromatic Al$K\alpha$ radiation was used as an exitation source ($h\nu$ = 1486.6 eV). During the measurement, the spectrometer was pumped to a residual pressure of about 10^{-9} Torr. The sample surfaces were mechanically scraped with a metal brush in the spectrometer, in order to expose fresh surfaces. The 1s binding energy of carbon, 284.6 eV, was used as an internal standard.

XANES experiments were carried out on beam line 10B at KEK-PF (Photon Factory, National Laboratory for High Energy Physics, Japan), operating at 2.5 GeV with ca. 300–360 mA of stored current. Samples were prepared in the form of layers of fine powder rubbed on the adhesive tape. To check the reproducibility of data, the first and second differentials of reference (Nb_2O_5) spectra were compared after each set of sample measurement.

Band calculations were carried out employing the extended Hückel tight binding (EHTB) method (37, 38).

Combustion analysis was carried out at 800°C in air; in this procedure $BaNbS_3$ was oxidized to $BaSO_4$ and $BaNb_2O_6$.

RESULTS AND DISCUSSION

X-Ray Diffraction Analysis

The products of nominal composition $BaNbS_3$ and $BaNb_{0.8}S_3$ were homogeneous black powders. The powder X-ray diffraction patterns of $BaNbS_3$ and $BaNb_{0.8}S_3$ were similar except for slightly different relative peak intensities. No extra peak was observed in $BaNb_{0.8}S_3$. However, very weak extra peaks at d = 6.21, 4.15, and 2.36 were observed in $BaNbS_3$, which were identified as the strong peaks of the $BaNb_2S_5$ phase (39). The major phase obtained from the starting composition $BaNbS_3$ was not $BaNb_{0.8}S_3$. It was previously reported (35) that the products are always nonstoichiometric, $BaNb_{0.8}S_3$, with an impurity phase, regardless of the starting reagent ratios of Ba/Nb. Even though the powder X-ray diffraction patterns of $BaNbS_3$ and $BaNb_{0.8}S_3$ were similar, the relative peak intensities were different. As shown in Fig. 1, the intensity ratios of the 110 and 021 reflections were strongly dependent on the compositions and were reproducible for two starting reagent ratios Nb/Ba. In Fig. 1, the four triangles indicate the I_{021}/I_{110} ratios for the nominal composition $BaNb_{0.8}S_3$, and the four circles represent those for $BaNbS_3$. The solid line indicates the theoretically calculated I_{021}/I_{110} ratios with varing Nb content and with fixed sulfur content. Within one standard deviation, the extrapolated composition of Nb agrees well with the starting composition in $BaNbS_3$, but it does not correspond to the starting composition of $BaNb_{0.8}S_3$. However, the niobium content was in complete agreement with the starting Nb/Ba ratio under the assumption that sulfur is deficient in $BaNb_{0.8}S_3$ (squares in Fig. 1). The dotted line indicates the theoretically calculated ratios

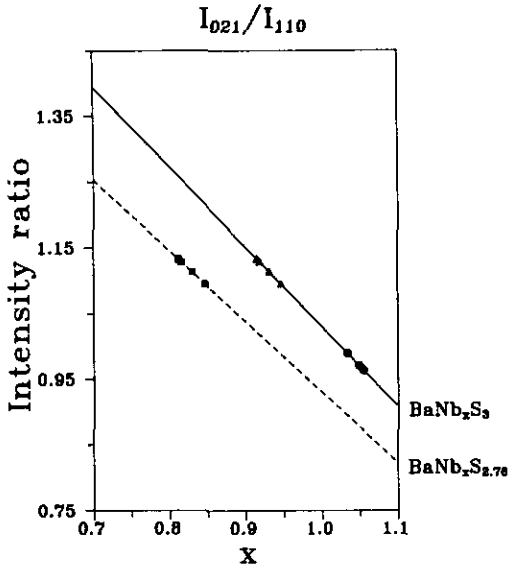

FIG. 1. Relative intensity ratios of 021 and 110 peaks of $BaNbS_3$ and $BaNb_{0.8}S_{2.76}$. *Solid lines indicate the calculated* I_{021}/I_{110} *ratios.* Triangles indicate the I_{021}/I_{110} ratios of four samples with nominal composition $BaNb_{0.8}S_3$ and circles indicate the I_{021}/I_{110} ratios of four samples with nominal composition $BaNbS_3$. The dotted line indicates the calculated ratios with 8% sulfur defect. Squares indicate the I_{021}/I_{110} ratios of four samples with $BaNb_{0.8}S_{2.76}$. Standard deviation of values is ~5%.

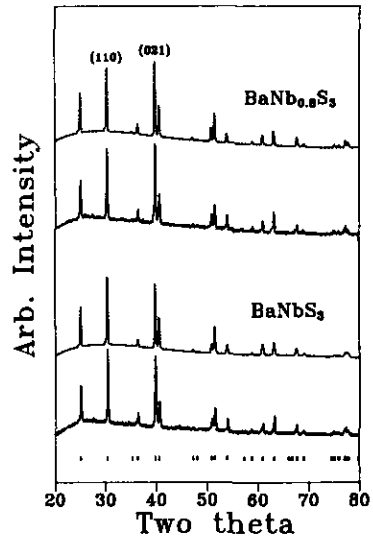

FIG. 2. Comparison of $BaNb_{0.8}S_3$ (top) and $BaNbS_3$ (bottom) powder diffraction. Vertical strokes indicate calculated Bragg peak positions. Dotted lines indicate calculated the patterns and the solids lines indicate the observed patterns.

with 8% sulfur defect, and this concentration of sulfur defect was obtained from the results of the Reitveld refinement (40) as described below. Rietveld-type full-profile refinement was carried out to obtain the scale factor, zero point, back ground parameters, thermal parameters, cell parameters, and atomic positions and occupancies (Fig. 2 and Table 1). The results of Rietveld analysis suggest that the sulfur octahedra are slightly expanded in $BaNb_{0.8}S_3$ (Nb–S distances = 2.529(2) Å) as compared to $BaNbS_3$ (Nb–S distance = 2.455(2) Å), and that the sulfur content of the $BaNb_{0.8}S_3$ phase is slightly deficient (i.e., $BaNb_{0.8}S_{2.76\pm0.02}$, hereafter denoted as $BaNb_{0.8}S_{3-\delta}$). The refinement results for the two compositions are in good agreement with the results of the combustion analysis. The resulting compositions of the $BaNbS_3$ and $BaNb_{0.8}S_{3-\delta}$ were $BaNbS_{3.04\pm0.02}$ and $BaNb_{0.8}S_{2.81\pm0.02}$, respectively.

XPS and XANES Experiments

XPS experiments were carried out to examine the oxidation state of niobium, in $BaNbS_3$ and $BaNb_{0.8}S_{3-\delta}$. The XPS spectra of $BaNbS_3$ contain an extra peak, which is considered to be that of the minor phase, $BaNb_2S_5$ (Fig. 3). Otherwise, the XPS spectra for the niobium 3*d* core levels of $BaNbS_3$ and $BaNb_{0.8}S_{3-\delta}$ were exactly the same.

TABLE 1
Refined Unit Cell and Atomic Parameters in $P6_3/mmc$

Composition	Atom	Position			Occupancy (%)	Thermal (Å²)
		x	*y*	*z*		
$BaNbS_3$	Ba	1/3	2/3	3/4	100(1)[a]	1.7614
	Nb	0.0	0.0	0.0	98(1)	1.7614
	S	0.1709(3)	0.3417(3)	1/4	100(1)	1.7614
$BaNb_{0.8}S_3$	Ba	1/3	2/3	3/4	100(1)	0.4103
	Nb	0.0	0.0	0.0	82(1)	0.4103
	S	0.1766(2)	0.3521(4)	1/4	92(2)	0.4103

Note. The hexagonal cell dimensions are $a = 6.840(2)$, $c = 5.745(2)$ Å for $BaNbS_3$ and $a = 6.836(2)$, $c = 5.748(2)$ Å for $BaNb_{0.8}S_3$. $R_{wp} = 3.8\%$ Overall isotropic temperature factors were used.
[a] Error.

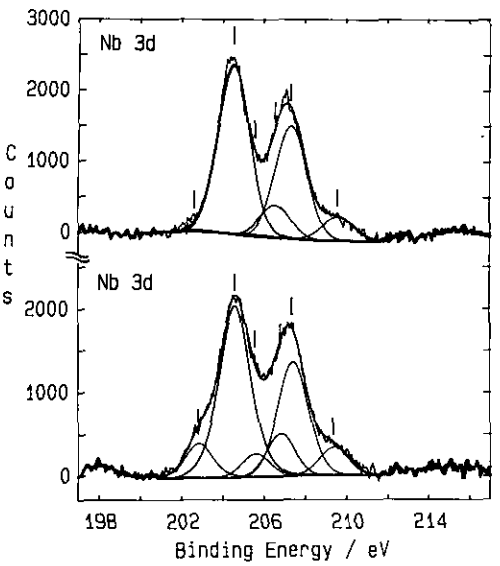

FIG. 3. Nb 3*d* core level XPS spectrum for $BaNb_{0.8}S_{3-\delta}$ (top) and $BaNbS_3$ (bottom).

Of the three peaks, the weak one at the highest binding energy disappeared after scraping the sample surface, which suggests that the highly oxidized species are present mainly on the sample surface. The three peaks could be resolved into two pairs of Nb $d_{3/2}$ and $d_{5/2}$ (Fig. 3, Table 2). The first doublet at 208.8 and 206.0 eV assigned to Nb^{5+} originates from the sample surface, and the second doublet at 207.2 and 204.5 eV assigned to $Nb^{4+\delta}$ originates from the bulk (41, 42). An extra doublet in $BaNbS_3$ appears to originate from the minor $BaNb_2S_5$ phase. The exact structure and niobium oxidation state of the $BaNb_2S_5$ phase are not known. $BaNb_2S_5$ may have a layered structure of alternating BaS and NbS_x (X = 1 or 2) layers.

TABLE 2
Niobium $3d_{3/2}$, $3d_{5/2}$ Binding Energy of $BaNb_xS_{3-\delta}$

Binding energy (eV)	FWHM (eV)	Area (%)	State
	(i) $BaNbS_3$		
209.4	1.67	6	$d_{3/2}$ (Nb^{+5})
206.8	1.61	9	$d_{5/2}$ (Nb^{+5})
207.4	1.81	28	$d_{3/2}$ ($Nb^{+4.x}$)
204.6	1.82	44	$d_{5/2}$ ($Nb^{+4.x}$)
205.6	1.57	5	$d_{3/2}$ (Nb^{+4})[a]
202.6	1.60	8	$d_{5/2}$ (Nb^{+4})[a]
	(ii) $BaNb_{0.8}S_{3-\delta}$		
209.6	1.84	7	$d_{3/2}$ (Nb^{+5})
206.5	1.78	9	$d_{5/2}$ (Nb^{+5})
207.3	1.81	33	$d_{3/2}$ ($Nb^{+4.x}$)
204.5	1.82	49	$d_{5/2}$ ($Nb^{+4.x}$)

[a] Nb^{4+} from $BaNb_2S_5$.

In order to obtain information about the oxidation state of the absorber atom in the bulk as well as the metal–ligand covalency, XANES experiments were carried out. Figure 4 exhibits the Nb*K*-edge XANES spectra of $BaNb_{0.8}S_{3-\delta}$ and $BaNbS_3$, including various reference compounds. Owing to the dipolar selection rule, the Nb*K* absorption edges are related to the local density of states of *p* character around the cations. It is clearly seen that the absorption edge shifts towards the lower-energy side as the oxidation state of the niobium decreases (from Nb_2O_5 to NbO_2, $BaNbO_3$ and sulfides). The Nb^{4+}-sulfide compounds exhibit the absorption edge at the lower-energy side compared to the Nb^{4+}-oxide compounds. This result is not surprising because, as one goes from oxide to sulfide, the effective charge on the niobium ion decreases due to greater covalency between metal ions and sulfur ligands. But the absorption edges of $BaNb_{0.8}S_{3-\delta}$ and $BaNbS_3$ are observed at slightly higher energies (~1.0 eV) than that of NbS_2 (in contrast, $BaNbO_3$ and NbO_2 show the same absorption edge). Thus the oxidation state of the niobium in $BaNb_{0.8}S_{3-\delta}$ and $BaNbS_3$ seems slightly higher than the tetravalent state. These XANES results are in good agreement with the XPS results discussed above. Note that there is no discernible shoulder below the absorption edge except for the case of Nb_2O_5. The shoulder is primarily associated with the dipole-forbid-

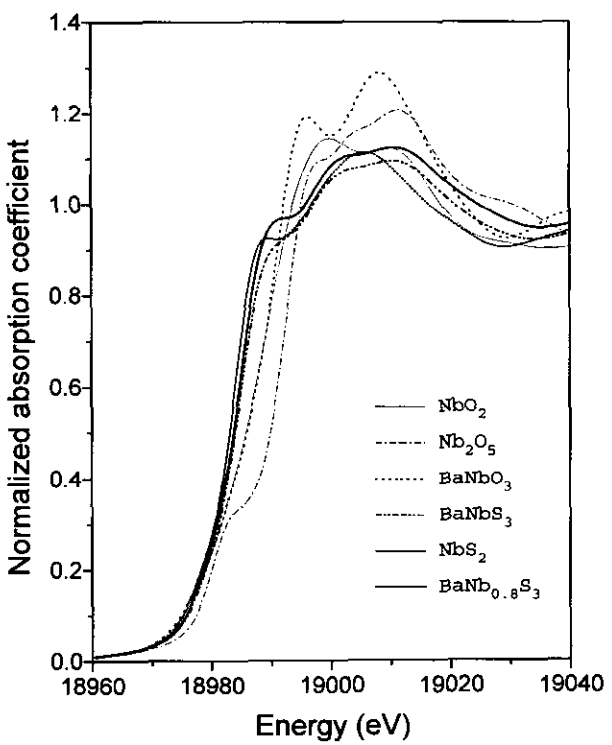

FIG. 4. Normalized Nb*K*-edge spectra of $BaNbS_3$, $BaNb_{0.8}S_{3-\delta}$, NbS_2, $BaNbO_{3-\delta}$, NbO_2, and Nb_2O_5.

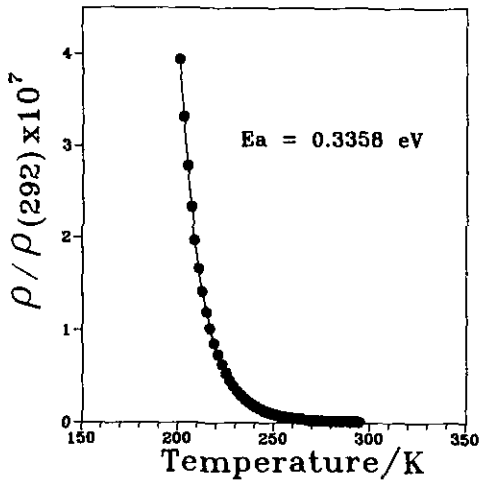

FIG. 5. Normalized resistivity as a function of temperature for $BaNb_{0.8}S_{3-\delta}$.

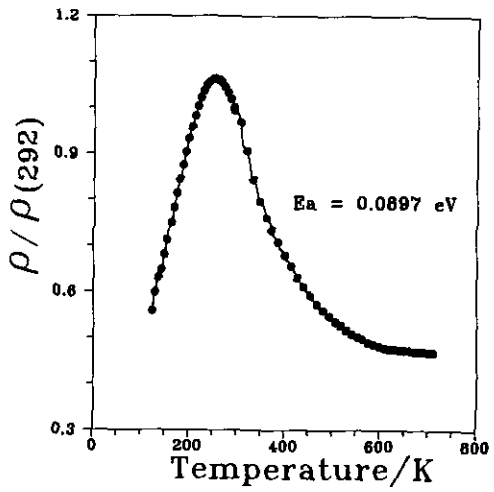

FIG. 6. Normalized resistivity as a function of temperature for $BaNbS_3$.

den $1s \rightarrow 4d$ transition, and, for compounds having centrosymmetric local environments with low oxidation states, the intensity of this peak becomes very weak. To obtain spectroscopic information on the *d* band structure of the transition metal, we are currently performing Nb- and $Ta L_{II,III}$-edge XANES studies for the system $BaMS_3$ (M = Nb, Ta). The latter involves the dipole-allowed transition from the atomic *p* state with a narrow core hole width to the *d* band.

Electrical and Magnetic Properties

The temperature dependency of the electrical resistivity for $BaNbS_3$ and $BaNb_{0.8}S_{3-\delta}$ is shown in Figs. 5 and 6. The $BaNb_{0.8}S_3$ phase showed semiconducting behavior; the activation energy was 0.3 eV with resistivity of 5.4×10^2 Ω cm at room temperature. For stoichiometric $BaNbS_3$, negative $d\rho/dT$ behavior above 240 K and positive $d\rho/dT$ behavior below 240 K were observed. The resistivity at room temperature was on the order of 8.9×10^{-2} Ω cm. For $BaTa_{1-x}S_3$ (x = 0.0, 0.2), similar $d\rho/dT$ behavior was observed. The activation energy of $BaTa_{0.8}S_3$ (nominal composition) was slightly larger (about 0.1 eV larger) than that of $BaNb_{0.8}S_3$. However, in the $BaNbS_3$ and $BaTaS_3$ phases, a small amount of metallic BaM_2S_5 (M = Nb, Ta) phase was present (less than 5%), and the reported resistivities of $BaNb_2S_5$ and $BaTa_2S_5$ were on the order of $\sim 10^{-3}$ and $\sim 10^{-4}$ Ω cm, respectively (39, 43). Considering the metallic properties of this impurity, the anomalous maximum in the resistivity seems to be due to this impurity phase, BaM_2S_5. Both the $BaTaS_3$ and $BaNbS_3$ systems are semiconducting at room temperature and are diamagnetic even though they have spins on their *d*-orbitals. The magnetic susceptibility data as a function of temperature suggest that $BaNbS_3$ is diamagnetic. The rapid increase of susceptibility at low temperature indicates that the compound contains a small amount of paramagnetic impurity (Fig. 7). Unlike diamagnetic $BaNbS_3$, $BaVS_3$ shows typical paramagnetic behavior down to 35 K and very weak ferromagnetic behavior below 35 K, as shown in Fig. 8. The magnetic moment calculated from the region following the Curie–Weiss law was 1.74 μ_B, which is close to the expected value from a $\frac{1}{2}$ spin localized on each V^{4+} (1.73$_{\mu B}$). Massenet and co-workers (8) have found that the magnetic properties of $BaVS_3$ are very sensitive to sulfur content. In stoichiometric $BaVS_3$, a transition from the paramagnetic to the antiferromagnetic state was reported to occur at 70 K (32). This magnetic behavior agrees well with the present results for $BaVS_{3-x}$ rather than with those for $BaVS_3$ (8).

The reason the isostructural $BaVS_3$ behaves differently

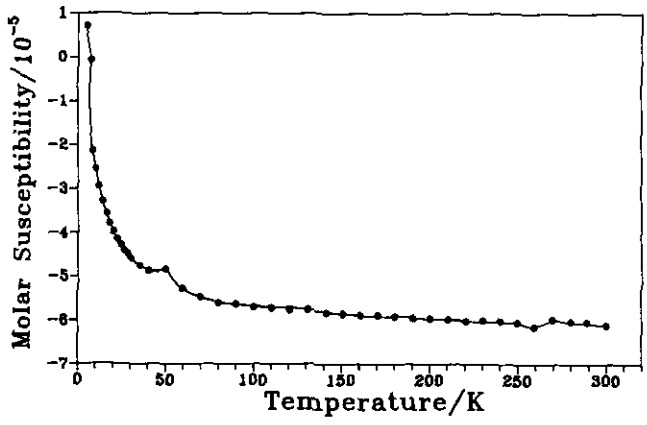

FIG. 7. Temperature dependence of magnetic susceptibility for $BaNbS_3$.

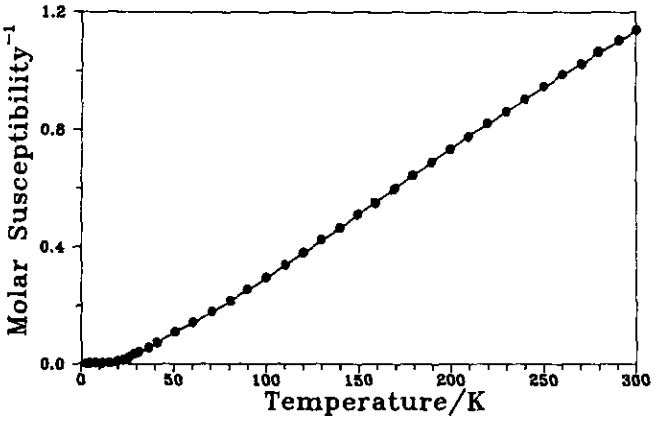

FIG. 8. Reciprocal magnetic susceptibility vs. temperature for $BaVS_{3-\delta}$.

from its congeners $BaNbS_3$ and $BaTaS_3$ could be understood based on the nature of their d electrons. Magnetic states are preferred when on-site repulsion (U) is greater than its bandwidth (W) (31). Here the d-block bandwidth depends on the degree of overlap of metal–metal or metal–nonmetal contacts. In Table 3, all metal–metal intrachains are compared to their sums of metallic radii, r_M (30). Notice that the interatomic distance of V–V is longer than $2 \times r_M$ (44(a)), while those of Nb–Nb and Ta–Ta are close to its respective values. For reference, V^{4+}–V^{4+} distance of VO_2 is 2.65 Å (44(b)). The average metal–metal distance of Ta_3S_2 is 2.91 Å, which is 0.02 Å shorter than that calculated from the Paulings bond order relation (44(c)), and the Ta–Ta single bond distance is 2.71 Å (44(d)). Therefore, the $3d$ electron in the VS_3^{2-} chain is more localized per metal atom throughout the chain than the $4d$ or $5d$ electron in NbS_3^{2-} or TaS_3^{2-} chain. Generally, although not invariably, the $3d$ metal–metal bond is weaker than the $4d$ or $5d$ bond (44(e)).

It is quite surprising that $BaMX_3$ (M = V, Nb, Ta), as nearly one dimensional materials with one electron per site, are not Peierls insulators at room temperature (33). Band calculation was carried out for an ideal MX_3^{2-} chain and for a system with pairing distortion. In the distorted chain, the M–M bond lengths were made to alternate in such a way that a cooperative Peierls distortion was

TABLE 3
Metal–Metal Bond Distances of Face-Sharing Octahedral MX_3^{2-} Chains

	$BaVS_3$	$BaVSe_3$	$BaNbS_3$	$BaTaS_3$
Intrachain	2.812	2.931	2.874	2.872
Interchain	6.712	6.999	6.836	6.846

Note. Distances are in Å.

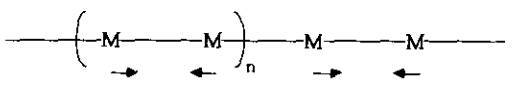

FIG. 9. The system with pairing distortion.

present (Fig. 9). The short metal–metal distances are made 0.2 Å shorter. Figure 10 shows the d-black bands of a typical MX_3^{2-} chain. The essential features of these bands were identical to those of the previous results (31, 45). The degeneracies at zone edge for ideal geometry in Fig. 10 are split off for the distorted geometry in Fig. 10. Consequently, 1a Nb^{3+} bands filled with two electrons are stabilized and their counterparts, 2a Nb^{5+} bands, are destabilized due to the gain and loss of bonding and antibonding character. Thus metals with $d^1 + d^1$ electrons in chain tend to pair up in a bonding band. Therefore, 2.6 kcal stabilization energy is gained for the chosen geometry. We have not optimized the distance due to the weakness of the EHTB method.

Even though our calculation shows energetic preference, such pairing distortion was not observed at room temperature and at a lower temperature (210 K). No su-

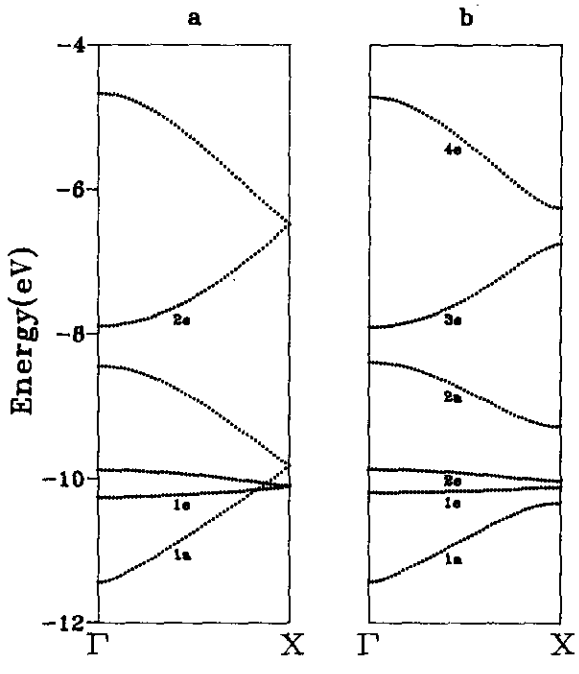

FIG. 10. (a) The d-block bands of a typical MX_3^{2-} chain are shown. For clarity, sulfur bands are not shown. The essential features of these bands are identical to those of previous results. The levels are with respect to the C_6 point group. In the calculation the z-axis is chosen for the chain axis for convenience, which is unusual for octahedral geometry, and every X–M–X angle is set to 90°. (b) The d-block bands calculated for the MX_3^{2-} system in the pairing distortion, in which the short metal–metal distance is 0.2 Å shorter.

perstructure peaks or lattice distortions were observed in the X-ray diffraction data, and only one $Nb^{4+\delta}$ NMR peak was observed at room temperature (46). These X-ray and ^{93}Nb NMR data agree well with the results of XPS and XANES as described above.

Therefore, structural distortion is not a major factor stabilizing the semiconducting state for $BaNbS_3$. The observed nonmagnetic semiconducting properties might be due to large spin–orbit coupling as in $BaTaS_3$ (Table 4) (36, 47–49). The eletrical conduction in the *d*-band involves electron transfer from one metal to another through a $d^1 + d^1 \rightarrow d^2 + d^0$ process. This process requires an energy U(on-site repulsion). In principle, spin–orbit coupling increases on-site repulsion (U), and this will stabilize the $d^1 + d^1(^2A_1)$ state relative to the $d^2 + d^0(^1A_1)$ state. This is the reason the (Nb or Ta)S_3^{2-} system prefers the $d^1 + d^1(^2A_1)$ state (Table 4). $BaMS_3$ (M = Nb, Ta) systems also have a wider width W of the *d*-bands than $BaVS_3$, which is a better condition for electron delocalization in $BaMS_3$ (M = Nb, Ta). However, conduction will occur if U is smaller than W; if U becomes larger than W, the compounds becomes a semiconductor. Therefore, $BaNbS_3$ and $BaTaS_3$ systems with large spin–orbit coupling prefer the semiconducting state, while the isostructural compound $BaVS_3$ prefers the metallic state. Also, the ground state of the d^1 ion in octahedral coordination is fourfold degenerate (Γ_8) state with zero magnetic moment ($g = 0$); thus it is diamagnetic.

In summary, $BaNb_{0.8}S_{3-\delta}$ and $BaNbS_3$ phases were synthesized. A small amount of impurity phase, $BaNb_2S_5$, affects the measurements of electrical properties in the $BaNbS_3$ phase. XANES experiments using Nb*K*-edges and XPS experiments proved that the oxidation state of Nb in these two phases was the same. It seems that the major factor stabilizing the semiconducting state for $BaTaS_3$ and $BaNbS_3$ is large spin–orbit coupling rather than structural distortion.

APPENDIX

All calculations employed the extended Hückel implemented tight binding method (37, 38). The Nb H_{ii} shown in Table 5 were obtained from the solid state charge iteration method. Orbital exponents were obtained from Clementi and Roetti (50). The property calculation used a 50 K point mesh. V–S bond distances are averaged.

TABLE 4
Spin–Orbit Coupling Constants for d^1 Transition Metals

λ unit	V^{4+}	Nb^{4+}	Ta^{4+}
eV	0.03	0.09	0.2
cm^{-1}	250	750	1610

TABLE 5
Parameters for EH Calculations

	Orbital	H_{ii}, eV	ξ_1[a]	ξ_2[a]	c_1[b]	c_2[b]
V	3*d*	−11.10	4.75	1.70	.4755	.7052
	4*s*	− 8.80	1.30			
	4*p*	− 5.80	0.90			
Nb	4*d*	−12.10	4.08	1.64	.6401	.5516
	5*s*	−10.10	1.89			
	5*p*	− 6.86	1.85			
S	3*s*	−20.00	1.82			
	3*p*	−13.30	1.82			

[a] Slater-type orbital exponents.
[b] Coefficients used in double-ξ expansion.

ACKNOWLEDGMENT

The present study was supported by the Ministry of Education Research Fund for Advanced Materials 1992 and in part by the Korean Science and Engineering Foundation (92-25-00-02). We thank Dr. H.-H. Park of ETRI for his help in the XPS experiments.

REFERENCES

1. L. A. Aslanov and L. M. Kova, *Russ. J. Inorg. Chem. (Engl. Transl.)* **9,** 1317 (1964).
2. R. A. Gardner, M. Vlasse, and A. Wold, *Inorg. Chem.* **8,** 2784 (1969).
3. R. A. Gardner, M. Vlasse, and A. Wold, *Acta Crystallogr. Sect. B* **25,** 781 (1969).
4. J. Huster, *Z. Naturforsch. B* **35,** 775 (1980).
5. M. Ishii and M. Saeki, *Phys. Status Solidi B* **170,** K49 (1992).
6. J. Kelber, A. H. Reis, Jr., A. T. Aldred, M. H. Mueller, O. Massenet, G. DePasquali, and G. Stucky, *J. Solid State Chem.* **30,** 357 (1979).
7. J. Kelber, J. D. Jorgensen, M. H. Mueller, O. Massenet, and G. D. Stucky, *Acta Crystallogr. Sect. B* **35,** 2473 (1979).
8. O. Massenet, R. Ruder, J. J. Since, C. Schlenker, J. Mercier, J. Kelber, and G. D. Stucky, *Mater. Res. Bull.* **13,** 187 (1978).
9. G. D. Stucky, C. Putnik, J. Kelber, M. J. Schaffman, M. B. Salamon, G. Pasquali, A. J. Schultz, J. Williams, T. F. Cornish, D. M. Washecheck, and P. L. Johnson, *Ann. N.Y. Acad. Sci.* **313,** 525 (1978).
10. M. Takano, H. Kosugi, N. Nakamura, M. Shimada, T. Wada, and M. Koizumi, *J. Phys. Soc. Jpn.* **43,** 1101 (1977).
11. M. Ghedira, J. Chenavas, F. Sayetat, M. Marezio, O. Massenet, and J. Mereier, *Acta Crystallogr. Sect. B* **37,** 1491 (1981).
12. H. T. Witteveen and J. A. R. van Veen, *J. Phys. Chem. Solids* **35,** 337 (1974).
13. H. T. Witteveen and J. A. R. van Veen, *J. Chem. Phys.* **58,** 186 (1973).
14. R. D. Willett, *J. Chem. Phys.* **45,** 3737 (1966).
15. G. D. Stucky, *Acta Crystallogr. Sect. B* **24,** 330 (1968).
16. H. Soling, *Acta Chem. Scand.* **22,** 2793 (1968).
17. J. Smith, B. C. Gerstein, S. H. Liu, and G. Stucky, *J. Chem. Phys.* **53,** 418 (1970).

18. A. W. Schlueter, R. A. Jacobson, and R. E. Rundle, *Inorg. Chem.* **5,** 277 (1966).
19. H. Rinneberg and H. Hartmann, *J. Chem. Phys.* **52,** 5814 (1970).
20. P. S. Peercy and D. Morosin, *Phys. Lett. A* **36,** 409 (1971).
21. M. Niel, C. Cros, M. Vlasse, M. Pouchard, and P. Hagenmuller, *Mater. Res. Bull.* **11,** 827 (1976).
22. B. Morosin and E. J. Graeber, *Acta Crystallogr.* **23,** 766 (1967).
23. G. L. McPherson and J. R. Chang, *Inorg. Chem.* **12,** 1196 (1973).
24. G. L. McPherson, T. J. Kistenmacher, J. B. Folkers, and G. D. Stucky, *J. Chem. Phys.* **57,** 3771 (1972).
25. I. E. Grey and P. W. Smith, *Chem. Commun,* 1525 (1968).
26. J. E. Fernandez, M. J. Tello, and M. A. Arriandiaga, *Mater. Res. Bull.* **13,** 477 (1978).
27. R. Dingle, M. E. Lines, and S. L. Holt, *Phys. Rev.* **187,** 643 (1969).
28. J. A. Ackerman, G. M. Cole, and S. L. Holt, *Inorg. Chim. Acta* **8,** 323 (1974).
29. N. Achiva, *J. Phys. Soc. Jpn.* **27,** 561 (1969).
30. J. B. Goodenough, "Magnetism and the Chemical Bond," Wiley, New York, 1963.
31. M. H. Whangbo, M. J. Foshee, and R. Hoffmann, *Inorg. Chem.* **19,** 1723 (1980).
32. K. Matsuura, T. Wada, T. Nakamizo, H. Yamauchi, and S. Tanaka, *Phys. Rev. B* **43,** 13,118 (1991).
33. R. E. Peierls, "Quantum Theory of Solids," Oxford Univ. Press, London, 1955.
34. G. D. Stucky, A. J. Schultz, and J. M. Williams, *Annu. Rev. Mater. Sci.* **7,** 301 (1977).
35. (a) P. C. Donohue and J. F. Weiher, *J. Solid State Chem.* **10,** 142 (1974); (b) B. H. Chen, G. Saghi-Szabo, B. W. Eichhorn, J.-L. Peng, and R. Greene, *Mater. Res. Bull.* **27,** 1249 (1992).
36. W. Geertsma, C. Haas, R. Huisman, and F. Jellinek, *Solid State Commun.* **10,** 75 (1972).
37. R. Hoffmann, *J. Chem. Phys.* **39,** 1397 (1963).
38. M. H. Whangbo, M. Evain, T. Hughbanks, M. Kertesz, S. Wijeyesekera, C. Wilker, C. Zheng, and R. Hoffmann, *QCPE Bull.* **9,** 61 (1989).
39. K. Matsuura, T. Wada, T. Nakamizo, H. Yamauchi, and S. Tanaka, *J. Solid State Chem.* **94,** 294 (1991).
40. A. Sakthivel and R. A. Young, "Program DBW9006PC for Reitveld Analysis of X-ray and Neutron Powder Diffraction Patterns," 1990.
41. D. Simon, C. Perrin, and P. Baillif, *C. R. Acad. Sci. Paris C* **241,** 283 (1976).
42. G. E. McGuire, G. K. Schweitzer, and T. A. Carlson, *Inorg. Chem.* **12,** 2451 (1973).
43. M. Saeki, H. Nozaki, and M. Onoda, *Mater. Res. Bull.* **24,** 851 (1989).
44. (a) P. Villars and L. D. Calvert, "Pearson's Handbook of Crystallographic Data for Intermetallic Phases," Am. Soc. Metals, 1985; (b) A. F. Wells, "Structural Inorganic Chemistry," 4th ed., Oxford Univ. Press, London, 1975; (c) L. Pauling, "The Nature of the Chemical Bond," 3rd ed., Cornell Univ. Press; Ithaca, NY, 1960; (d) W. B. Pearson, "The Crystal Chemistry and Physics of Metals and Alloys," Wiley–Interscience, New York, 1972; and (e) F. A. Cotton and R. A. Walton, "Multiple Bonds Between Metal Atoms," Wiley, New York, 1982.
45. M. Charlot, J. J. Girerd, and O. Kahn, *Phys. Status Solidi B* **86,** 497 (1978).
46. S.-J. Kim, A.-J. Woo, and L. G. Butler, In preparation (1994).
47. M. H. Whangbo, *Inorg. Chem.* **19,** 1728 (1980).
48. M. H. Whangbo, *J. Chem. Phys.* **70,** 4963 (1979).
49. A. H. Thompson, F. R. Gamble, and J. F. Revelli, *Solid State Commun.* **9,** 981 (1971).
50. E. Clementi and C. Roetti, *At. Nucl. Data Tables* **14,** 177 (1974).